2015

Microstructural Analysis of Aluminum High Pressure Die Castings

Maria Diana David
University of Alabama at Birmingham

MICROSTRUCTURAL ANALYSIS OF ALUMINUM HIGH PRESSURE DIE CASTINGS

by

MARIA DIANA DAVID

CHARLES MONROE, COMMITTEE CHAIR
ROBIN FOLEY
JOHN GRIFFIN

A MASTER THESIS

Submitted to the graduate faculty of The University of Alabama at Birmingham,
in partial fulfillment of the requirements for the degree of
Master of Science

BIRMINGHAM, ALABAMA

December 2014

MICROSTRUCTURAL ANALYSIS OF ALUMINUM HIGH PRESSURE DIE CASTINGS

MARIA DIANA DAVID

MATERIALS SCIENCE AND ENGINEERING

ABSTRACT

Microstructural analysis of aluminum high pressure die castings (HPDC) is challenging and time consuming. Automating the stereology method is an efficient way in obtaining quantitative data; however, validating the accuracy of this technique can also pose some challenges. In this research, a semi-automated algorithm to quantify microstructural features in aluminum HPDC was developed. Analysis was done near the casting surface where it exhibited fine microstructure. Optical and Secondary electron (SE) and backscatter electron (BSE) SEM images were taken to characterize the features in the casting. Image processing steps applied on SEM and optical micrographs included median and range filters, dilation, erosion, and a hole-closing function. Measurements were done on different image pixel resolutions that ranged from 3 to 35 pixel/μm. Pixel resolutions below 6 px/μm were too low for the algorithm to distinguish the phases from each other. At resolutions higher than 6 px/μm, the volume fraction of primary α-Al and the line intercept count curves plateaued. Within this range, comparable results were obtained validating the assumption that there is a range of image pixel resolution relative to the size of the casting features at which stereology measurements become independent of the image resolution. Volume fraction within this curve plateau was consistent with the manual measurements while the line intercept count was significantly higher using the computerized technique for all resolutions. This was attributed to the ragged edges of

some primary α-Al; hence, the algorithm still needs some improvements. Further validation of the code using other castings or alloys with known phase amount and size may also be beneficial.

Keywords: dendrites, stereology, microscopy

ACKNOWLEDGMENTS

I would like to express my sincere gratitude and appreciation to my advisor and committee chairman, Dr. Charles Monroe, for the continuous support and encouragement throughout my graduate study. His insightful comments and ideas on this research as well as other projects I had the opportunity to work on and his unwavering enthusiasm pushed me to think more critically and made me realize how exciting learning can be.

I also would like to thank Dr. Robin Foley who has been tremendously supportive of my academic and research activities from my undergraduate days up to now. Her motivation and immense knowledge in metallurgy inspired me to pursue a graduate degree. My deepest gratitude also goes to Mr. John Griffin for his patience and commitment in sharing his vast experience and knowledge on metal castings with us graduate students. His resourcefulness and professionalism motivated me to become a better engineer.

Special thanks to: Dr. Brian Pillay for providing feedback during my thesis defense and for the support and belief in me ever since I was an undergraduate, and William Monroe for his time and patience in creating and modifying the algorithm I used in this research and sharing his knowledge on SEM and image analysis.

I would never have survived my graduate study without my labmates in the casting group, both past and present: William Warriner, Sid Biswas, Alex Noble, Nic Willis, Rhiannon Bragg, Chunlei Wang, Jun Ge, Carlos Colina, Elis Rivera, and Jit

Chakraborty. Their company and insights on academic, professional, and personal matters have made graduate school more meaningful and memorable. My gratitude also goes to Kristin Hardin, Alejandra Constante, and all the other members of the MSE department who have been a part of both my undergraduate and graduate life at UAB.

Finally, I want to thank my parents, sisters, and friends for the never ending support and inspiration.

TABLE OF CONTENTS

page

LIST OF TABLES

LIST OF FIGURES

1. INTRODUCTION

High pressure die casting (HPDC) offers the advantage of producing complex parts in a short casting cycle time. There are two conventional die casting processes: the hot chamber and the cold chamber.

In a hot chamber die casting machine, the metal injection system is in contact with the molten metal at all times. Die filling is typically between 5 to 40 msec[1]. Since the injection system is immersed in the melt, this process is only used for metals with low melting temperature such as lead and zinc alloys[1].

In cold chamber HPDC, superheated metal is poured into a shot chamber. The melt is pushed into the runners up to the gates and then injected through the gates at high velocity, typically 50 ms^{-1}[2]. To aid feeding of the solidification shrinkage, a pressure of 20 to 100 MPa is applied to the metal near the end of solidification[2]. The cold chamber HPDC is typically used for brass and aluminum alloys.

Due to the relatively high cooling rates, HPDC alloys have a finer microstructure compared to other casting processes; hence, good mechanical properties can be attained. However, die castings typically exhibit a nonhomogeneous microstructure which limits their applications to nonstructural components.

The most common microstructural feature found in die castings is porosity. This can either be due to solidification shrinkage or gas entrapment[1]. Most metals decrease in volume by about 7% during solification. If this decrease is not fed with additional liquid metal, shrink porosity will result. High metal velocities can mix the metal with air which can be entrapped in the solidifying material. Other microstructural features include

intermetallics such as an iron-rich phase, sometimes referred to as sludge, which can be found depending on combination of temperature and composition and other processing conditions.

Other features have been observed and reported: (1) skin layer; (2) defect/shear bands; and (3) externally solidified crystals (ESCs). These features are typically localized in a region but can sometimes be uniformly distributed throughout the casting.

The skin layer exhibited by most die castings can be (1) a primary product size modified zone, (2) a primary solidification product depleted zone, or (3) a porosity-free zone near the mold-metal interface or surface of the casting[3]. Sannes et al.[4] defines this layer as the material that rapidly solidified along the die walls. This region becomes stationary as they reach a solid fraction that is strong enough to resist flow of the incoming material[4].

Defect bands generally contain a relatively higher amount of solute than the bulk composition[5]. They were found to exist in both hot chamber and cold chamber HPDC[2].

ESCs have a wider definition in published works. Some research works consider aluminum oxide inclusions or films and sludge which generally contains Fe, Mn, and Cr as ESCs[3]. The general description of ESCs states that they are primary solidification products that formed in the shot sleeve and injected into the die cavity during filling[3,5].

Due to the complex flow and solidification mechanisms that occur in a die casting process, acquiring real time process variables is challenging. Instead, analysis of the resulting microstructure has been done to further understand this casting process.

Methods of quantifying features in a casting may typically involve comparison to charts or images with known values, manual measurements using image analysis tools, or

measurements using a computerized image analysis method. Since there is limited data on aluminum die castings, microstructural analysis can be done using either the manual or the computerized measurement techniques.

Both manual and automated measurements require sets of images that show representative areas of the casting. Due to the human ability to distinguish artifacts in an image, manual measurements are less sensitive to image quality. However, bias and error are still inevitable; the operator may select a feature or an area that does not represent the entire region or the casting being examined and, especially for die castings, fine features may be missed. The computerized technique is more sensitive to the quality of the image, on the other hand, but certain image processing techniques can be applied to control this. In addition, bias and error can be minimized in an automated measurement technique. Due to the fine and nonhomogeneous characteristics of the microstructure, manual stereology method tends to have lower precision and efficiency. Automated quantitative technique, once validated, can lead to more precise results in a timely manner.

An image is basically a grid of pixels which individually correspond to either a single gray level intensity or color value. This characteristic of images makes application of processing techniques using various mathematical functions possible. It must be noted that a computerized analysis must be done with significant care to avoid altering the original image leading to inaccurate results.

To eliminate or, at least, lessen unnecessary features, image noise must be reduced. One method of reducing image noise is by using a median filter. The pixel of interest is replaced by the median value of its neighboring pixels. This neighborhood is

defined by a filter window which moves through the whole image pixel by pixel. The input value sets the size of this window so its value can be any odd integer greater than 1.

In order to distinguish important features from each other, boundaries that separate them must be determined. Range filter is one way to detect these edges in an image. Similar to the median filter, a square filter grid moves through the image and replaces the central pixel with the range (i.e., difference between maximum and minimum) of the values in the filter window. The size of the range filter can be defined by any odd integer greater than 1.

Since the automated technique that will be presented must be validated accordingly, simplification of the microstructure to a binary system (i.e., 2 phase microstructure) is ideal. To further segment the microstructure into these 2 features, the image must be converted to a binary image. Referred to as thresholding, the pixel values of the image, which typically range from 0 to 255 for grayscale images, are replaced by either 0 or 1 depending on the conversion method used. The output pixel of 0 corresponds to a black feature and 1 to a white phase.

The most basic morphological operations in image analysis are dilation and erosion. In dilation, the pixel of interest will be replaced by the maximum value (i.e., 1 for binary images) of its neighborhood. Erosion, on the other hand, replaces the central pixel with the minimum value (i.e., 0 for binary images) of its neighboring pixels. The neighborhood for these functions is defined by the structuring element which can vary in size and shape – both can be defined in the algorithm. These elements can range from a line, square, diamond, disk, or ball. Similar to the filter windows previously mentioned, these structuring elements move through the whole image.

For an Al-Si die casting with a eutectic microconstituent, dilation or erosion can transform the two-phase (i.e α-Al and Si-rich layers) eutectic lamellae into a single feature. The structuring element moves through these eutectic layers and converts the pixel values of the α-Al layers within these eutectic networks to the pixel values of the Si-rich layers. For an SEM image where the α-Al appears darker relative to the other features, dilation will result in the α-Al eutectic layers (i.e., value of 0) being converted to Si-rich eutectic layers (i.e., value of 1) in terms of the pixel values. The algorithm will count the eutectic regions as a single bright phase instead of alternating layers of bright and dark phases. In an optical micrograph, the α-Al is relatively brighter so erosion may be used to transform the eutectic region into a single phase component. If the optical image will be dilated instead, inversion of the pixel intensity values of the image may be done to achieve similar eutectic lamella transformation in an eroded image.

1.1. Background

The skin layer is typically free of porosity and is either α-rich or solute rich. Gourlay et al.[2] examined AlSi7Mg and AM- and AZ-series magnesium die castings. There was no skin layer in the aluminum casting while a distinct skin with a non-uniform thickness skin containing high amounts of ESCs was found on AM60 and AZ91. ESCs may have been trapped within the surface layer by the solidifying material. Chen[6] characterized the microstructure of Al-11Si-2Cu-Fe cast using two dies with different thickness and shape. Along surfaces that were parallel to the flow, a porosity-free, fine α-Al-rich layer was found. In surfaces that experienced low impact of incoming metal during filling, a combination of α-Al and fine eutectic formed before α-Al-rich layer. This surface layer is similar to the normal α-eutectic microstructure within the casting but

is finer. The subsequent α-Al-rich layer was observed to be thinner when it is farther away from the cast surface. There was no α-Al-rich skin layer observed on regions of direct melt impingement (i.e., die surface normal or close to normal to the flow direction). Otarawanna et al.[5] analyzed the microstructural features of AlSi4MgMn and AlMg5Si2Mn by casting them into tensile test bars with a 30-mm gage length and a total length of 125 mm. There was relatively more eutectic along the cast surface. In addition, the primary α-Al in the surface layer is finer than the bulk of the casting.

Defect bands generally exhibit localized positive segregation[5] and contain a larger amount of phase that form late as the casting solidifies[2]. For Al-Si alloys, which will be discussed later, these bands contain Al-Si eutectic. Defect bands can form either near to or far from the cast surface[2]. They are often continuous over the length of the casting and can sometimes extend from the runners[7] to the overflows[8], and they generally follow the surface contour in the bulk flow direction[2]. They also tend to form at corners or at abrupt changes in cross-sectional areas and in regions of unidirectional flow[7,8]. Porosity and torn regions can also be found in these bands especially in Mg-Al systems[7-9].

Gourlay et al.[2] proposed that defect bands exhibit the same characteristics as the dilatant shear bands observed in rheology studies[10,11] and laboratory gravity experiments[12]. Dilatant shear bands form when a solid network experiences local shearing and expands while they are sheared. Solute-rich liquid is drawn in the band as it forms which causes positive segregation[2]. The high densification pressure is also believed to subject the solidifying material to shear stresses[5].

Gourlay et al.[2] examined AM60, AZ91, and AlSi7Mg and found distinct bands of porosity that followed the surface contour of magnesium alloys and no bands of pores in

Al-Si alloys. There were, however, bands that exhibit positive segregation for all the alloys. The defect bands on the gage section of AlSi4MgMn and AlMg5Si2Mn tensile test bars mainly consisted of solute-rich regions[5]. These bands were almost parallel along the cast surface over the length of the gage section.

ESCs form in the shot sleeve, and they are injected into the die cavity during filling[5]. They are significantly larger than the in-cavity solidified grains due to the lower cooling rate in the shot sleeve relative to the cooling rate of the metal within the mold. ESCs can either be dendritic or globular[5] and have a slight tendency to be in the center of the casting. Laukli et al.[9] reports that this is caused by the shear induced migration of ESCs from high to low sheared regions during filling.

Higher amount of ESCs were found to be concentrated along the centerline of Mg HPDC while there were very few ESCs that are uniformly distributed throughout the casting for Al alloys[2]. Otarawanna et al.[5] reported smaller fraction of ESCs at locations farther from the gate in aluminum die castings. There are fewer ESCs farther from the gate because there are relatively more ESCs formed near the water-cooled plunger tip than in regions far away from it; thus, there are less ESCs in the first metal injected into the cavity. The majority of the ESCs were concentrated along the centerline of the casting. ESCs were present in both branched-dendritic and globular-rosette morphology while the in-cavity α-Al exhibited an equiaxed globular-rosette morphology.

Although there were early speculations that the formation of ESCs and defect bands in die castings are mutually inclusive, Rodrigo and Ahuja[8], Laukli et al.[13], and Gourlay et al.[2] found defect bands in Mg-Al and Al-Si alloys with little to no ESCs.

Otarawanna[5] observed significant amount of porosity in aluminum die castings that were about 100 μm in diameter. Both gas and shrinkage pores were localized along the centerlines of thin castings[6]. Other intermetallics, such as the iron-rich phase commonly referred to as sludge, are also typically found locally concentrated or uniformly distributed throughout the casting[5,6].

Various parameters control the formation of these microstructural features. Pitsaris et al.[7] reported that the pouring temperature and the filling velocity have the largest effect. Increasing the pouring temperature leads to less ESCs or porosity in the defect band while a high filling velocity results in a band closer to the cast surface. Although there is no effect on the band position, Rodrigo and Ahuja[8] claim that a high intensification pressure makes the defect band more distinct, and it also significantly reduces the porosity within the casting[6]. A high filling velocity leads to a higher impact pressure on the die surface which should increase the heat flow rate. Increasing the intensification pressure would also increase the heat transfer coefficient[6]. Both circumstances would cause formation of fine grains along the die walls. For Al-Si alloys, high pressure increases the melting temperature (T_m) of aluminum and decreases silicon's T_m[6]. Under pressure, eutectic point shifts toward the element with less increase in T_m (i.e., Si); thus, increasing the pressure should increase the α-Al for hypoeutectic alloys[6]. The amount of ESCs can be partially controlled by altering the melt superheat or shot delay time, by heating or insulating the shot sleeve, or changing the shot chamber fill fraction[2].

Various methods have been used in an attempt to characterize and quantify these features. Traditional stereology methods are done by analyzing micrographs and

conducting manual measurements. The grain size and DAS[14,15] can be measured using the line intercept method, where the number of dendrite arm spacing intercepts counted is divided by the total length of the line[16,17]. Electron Back-Scattered Diffraction (EBSD) has also been used to measure grain size[18]. This technique, however, can be time consuming as it requires a demanding sample preparation and significant scanning electron microscope time. Measurement of hardness and alloy content of different regions has also been used to analyze the microstructure of die castings. Weiler[19] characterized the skin layer by measuring the microhardness, the amount of eutectic, the amount of aluminum and oxygen content, and change in grain size across the thickness of the casting. The skin layer was reported to be generally harder than the other areas[6, 20]. However, hardness profile does not give an accurate determination of thickness of the skin layer[21].

1.2. Problem Statement

Due to the coupling of flow, heat transfer, and solidification mechanisms at extremely high rates, it is quite challenging to acquire real time data for die castings. Consequently, the relationship between process parameters and the resulting microstructure has not been fully understood. To narrow this knowledge gap and, ultimately, improve the mechanical properties attainable, researchers have been analyzing the microstructure of various die castings. However, quantitative analysis on die castings still poses some difficulty due to the fineness and non-homogeneity of their microstructure. In addition, there are limited published data on aluminum HPDC which limits the degree of validation on any experimental measurements. Thus, there is still a need to quantify and to contribute to the set of data on the microstructure of aluminum

die castings. In this research, a robust and efficient quantitative characterization method was developed.

1.3. Objectives

Manual measurements on the volume fraction and dendrite arm spacing on aluminum die castings can be challenging and time consuming due to its fine and non-homogeneous characteristics. Thus, a semi-automated technique which involves image analysis using programming software will be proposed. Aside from decreasing the number of measurements needed to achieve a good coefficient of variation, the results will be reproducible and analysis time will be much shorter.

Various image processing parameters that may affect the measurements will be considered. Their individual effects on the output measurements and recommended value range for each of them will be presented. The length scale or resolution necessary to distinguish features will also be determined. The output values measured by the algorithm will be compared to manual measurements.

2. MATERIALS AND METHODS

Microstructural analysis was done on an aluminum 380 die casting. Micrographs of the sectioned sample were taken using Axioplan 4MP optical microscope and FEI FEG-650 SEM Scanning Electron Microscope (SEM) equipped with an EDAX TEAM SDD 30mm^2 energy dispersive x-ray detector (EDS). The major phases found in EDS scans were (1) primary α-Al, (2) Al-Si eutectic, and (3) Fe-rich intermetallics which are noted in Figure 1. To simplify the image analysis, the sample was treated as a binary system: (1) primary α-Al; and (2) eutectic + intermetallics. All the images were taken

within 80 to 400 μm from the cast surface. This variation in location is due to the difference in total image area for different magnifications.

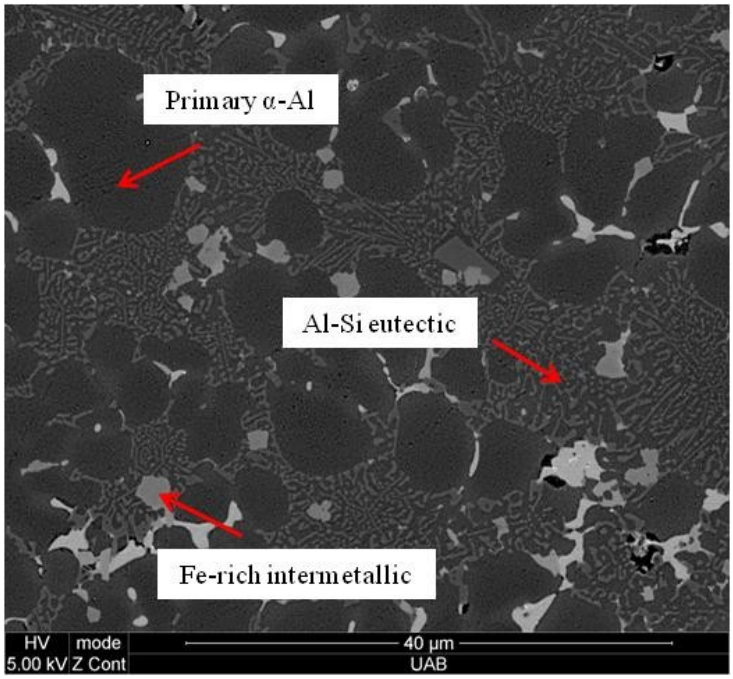

Figure 1. Backscatter electron SEM image showing the major phases found in the aluminum 380 high pressure die casting examined.

Manual measurements were done on secondary electron SEM images using ImagePro Plus™ image analysis software. Volume fraction (V_v) was measured using the point count method (see Equation 1). Line intercept method (see Equation 2) was done using a circular grid mask. The line intercept count in Equation 2 was used to calculate the λ_{alpha} or the thickness of the primary α-Al and $\lambda_{eutectic}$ or the thickness of the eutectic. Equations 3 and 4 show how these values were calculated.

$$V_v = \frac{\#\ of\ intercepts}{total\ number\ of\ points} \qquad (1)$$

$$P_L = \frac{\#\ of\ intercepts}{total\ length\ of\ grid} \quad (2)$$

$$\lambda_{alpha} = \frac{(4 \times V_v\ of\ alpha)}{(2 \times P_L)} \quad (3)$$

$$\lambda_{eutectic} = \frac{(4 \times V_v\ of\ eutectic)}{(2 \times P_L)} \quad (4)$$

The automated image analysis was done using Matlab[22]. A schematic diagram of the algorithm process is presented in Figure 2. Since some intermetallics cannot be distinguished from the α-Al regions in a secondary electron (SE) image, the algorithm required two images as input: the SE and backscatter electron (BSE) images. For the analysis on the optical micrographs, the same image was used for this required input. The input image size is the length scale or image resolution in terms of pixel per micron. In addition to the micrograph and its corresponding image size, values of each processing parameter used by the algorithm were defined before each run. These image processing parameters were (1) noise reduction, (2) edge detection, (3) dilation and erosion, and (4) hole close.

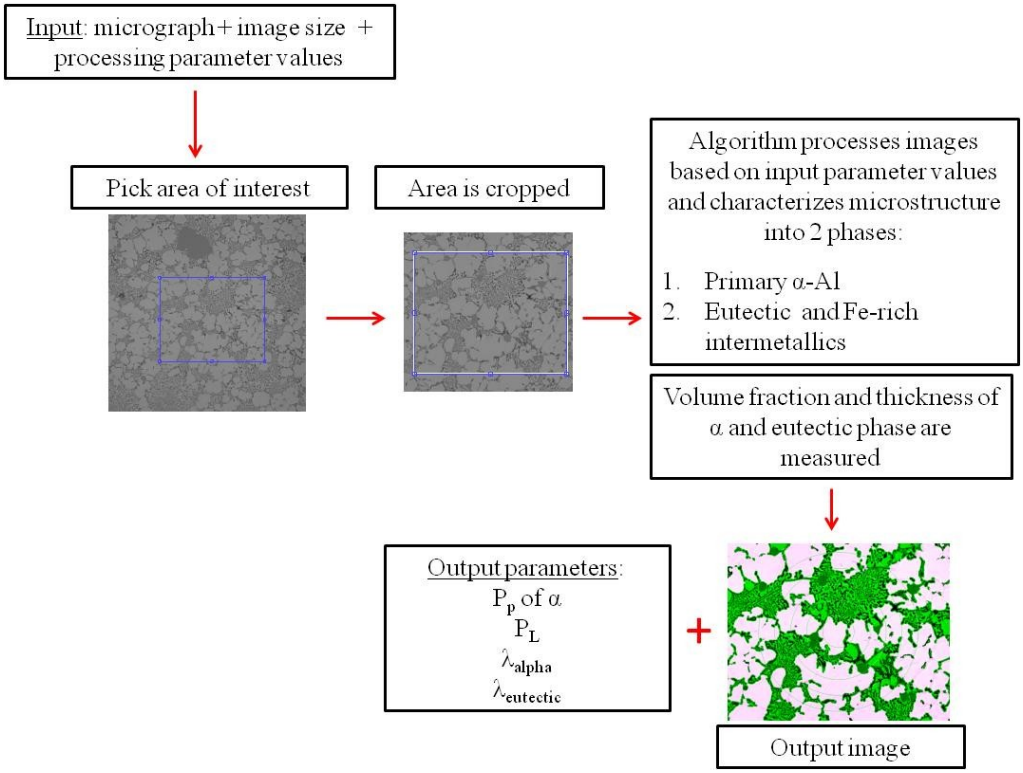

Figure 2. Schematic diagram of computer-aided microstructural analysis.

To minimize unnecessary features in the analysis, image noise was removed in the first step. A median filter was used since it is not too sensitive to outliers; hence, it will less likely to eliminate fine but important features. For SEM analysis, this step was done on both secondary electron (SE) and backscatter electron (BSE) SEM images. The images were padded with zeros along its edges so the outermost pixels can be processed.

To start distinguishing the eutectic and primary α-Al from each other, edges surrounding them were detected using the function range filter. For SEM analysis, this step was done on the SE image after applying the median filter.

The image was converted to a binary image. The image from the edge detection step was thresholded using Otsu's method[23] where a global threshold is calculated.

Dilation was done on the thresholded image from the previous step. The structuring element used for the dilation and erosion was a disk. The input pixel value set its radius. It is important to note, however, that for values less than 4 pixels, unless specified, the defined radius may create various shapes instead of a disk. During this step, each eutectic lamella (i.e., appears white in the binary image) expanded reducing the gaps in between them.

After dilating the eutectic phase, some small holes that still existed within the eutectic regions were removed based on their connectivity. The connectivity defined in this case was 8 which means that any pixel was considered connected to another pixel if they were connected horizontally, vertically, or diagonally. Small holes were removed in the α-Al and eutectic regions.

After completely filling in the gaps within the α-Al and eutectic, erosion was performed on the binary image. In this step, α-Al – eutectic boundaries that expanded from dilation were recovered. It must be noted that this is not always the case if the structuring element is a disk because some straight edges or corners may have rounded off during dilation.

Small intermetallics within the α regions were removed during the hole-closing step; therefore, inclusion of the BSE image was necessary. As previously mentioned, the median filter was also applied to the BSE image. It was thresholded using the graythresh function. Dilation and erosion was done on the binary BSE image. The eroded image was then combined with the eroded SE image.

Before the algorithm produced the output image, the binary image was inverted (i.e., eutectic changed from white to black phase and α-Al changed from black to white

phase). To check the quality of the image processing steps, the output image was overlaid to the input SE image with the α-Al phase highlighted in pink and eutectic in green.

Figure 3 summarizes all the image processing steps described in the previous text.

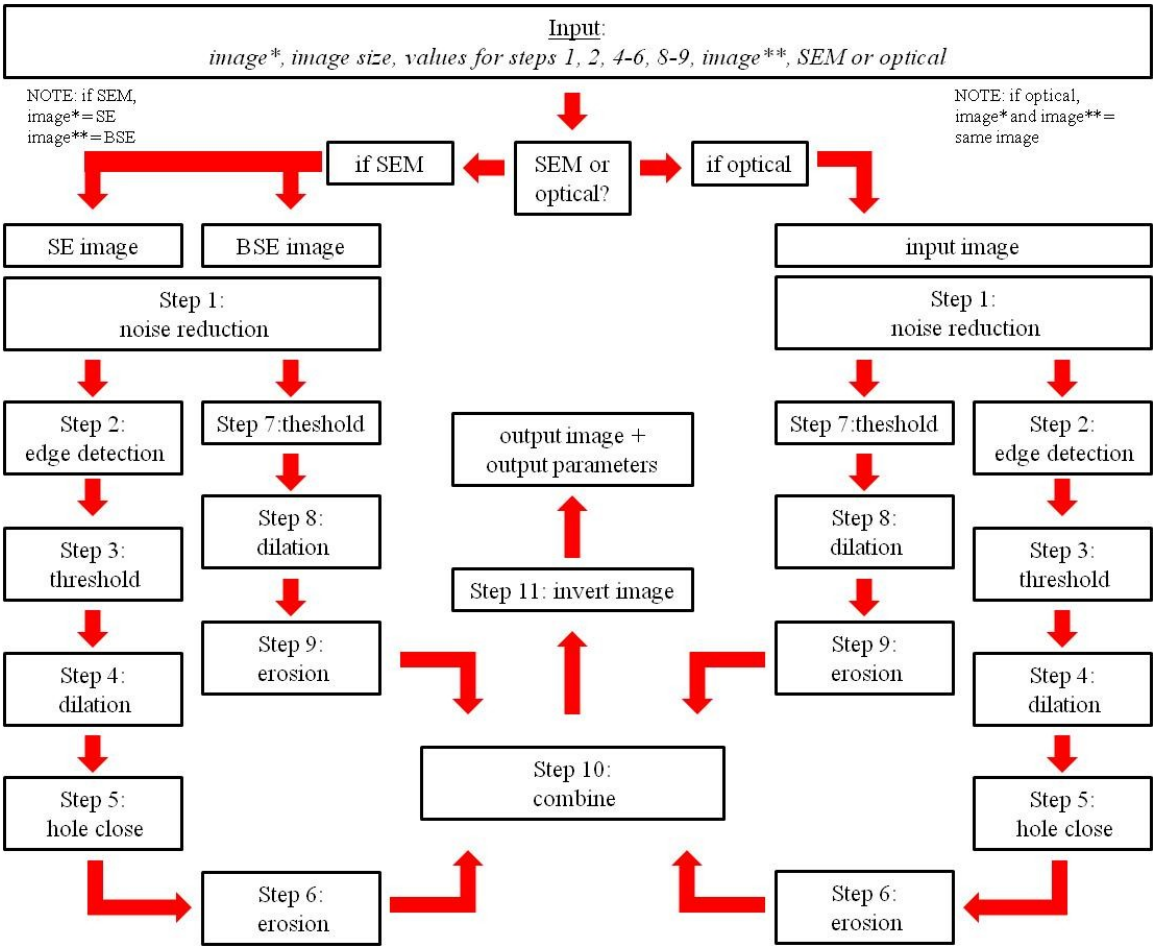

Figure 3. Detailed schematic diagram of algorithm showing steps done to analyze SEM and optical images.

2.1. Parameter Study

To determine the effects of each image processing parameter to the measured results, studies were done in which each parameter was treated as a variable while the other three were held constant. Table 1 shows the range of values used.

Table 1. Values Used for Each Parameter Study

Variable	Parameter Values			
	Noise Reduction, µm	**Edge Detection, µm**	**Dilation/ Erosion, µm**	**Hole Close, µm^2**
Noise Reduction	0.06 – 3	0.3	0.3	120
Edge Detection	0.3	0.1 – 3	0.3	120
Dilation/Erosion	0.3	0.1	0.06 – 6	120
Hole Close	0.3	0.1	0.3	30 – 6000

2.2. Output Parameters as a Function of Length Scale

From the parameter studies, specific values for each parameter were chosen. Different magnifications of SEM and optical images were analyzed. Table 2 summarizes the corresponding pixel resolution for the set of images used. Unless specified, 10 images were measured at each magnification. To compare the algorithm's measurements, manual measurements were done on a representative image for each pixel resolution.

Table 2. Corresponding Pixel Resolution for Each Magnification Analyzed

	Magnification	Length Scale or Pixel Resolution, px/μm
SEM	1000	3.4
	2000	6.9
	4000	13.7
	5000	17.2
	6000	20.6
	10000	34.3
optical	200	2.6
	500	6.5
	1000	13.2

3. RESULTS AND DISCUSSION

3.1. Parameter Study

For this analysis, only one set of images (i.e., SE and BSE) was used as shown in Figure 4. This image was taken at 5000x with an image size of 2048 by 1768 px. Its corresponding length scale is about 34.3 px/μm.

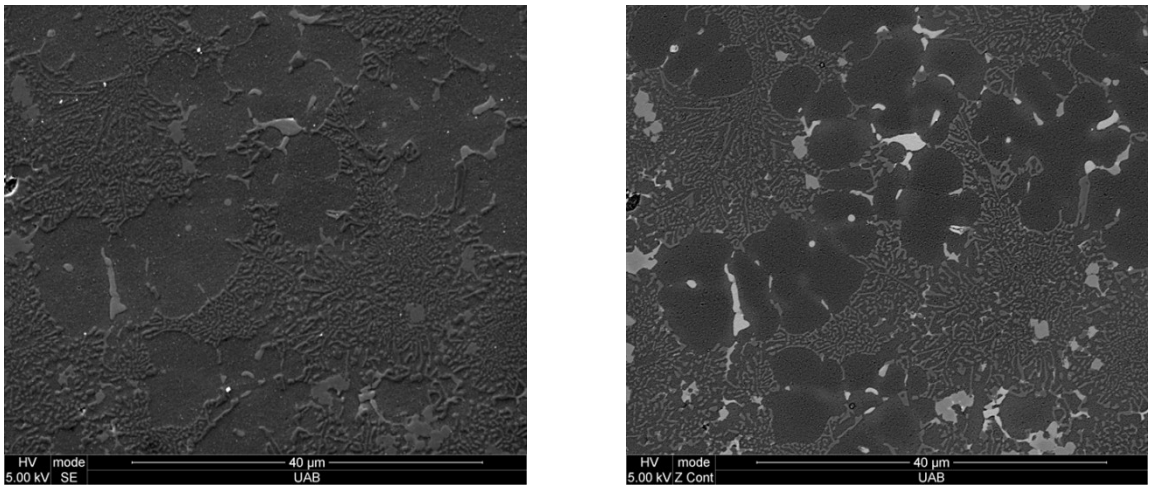

(a) (b)

Figure 4. (a) Secondary electron and (b) backscatter electron (right) SEM images used in the parameter studies.

3.1.1. Noise Reduction

The range of values used is presented in Table 3.

Table 3. Values Used for Parameter Study with Noise Reduction as a Variable

Noise Reduction		**Edge Detection**		**Dilation/Erosion**		**Hole Close**	
µm	px	µm	px	µm	px	μm^2	px^2
0.6 – 3	3 – 101	0.1	5	0.3	10	120	4096

Figures 5a and 5b show the volume fraction and line intercept count as a function of the noise reduction value. There was no primary α-Al measured at the onset of the curve and, then, the α-Al measurements sharply increased with the noise reduction parameter value. The volume fraction curve plateaus while the line intercept count curve does not exhibit a similar behavior. Figures 6 to 8 show the comparison of two data

points on these curves: a 0.1µm by 0.1µm (5 px by 5 px) median filter and a 0.6µm by 0.6µm (21 px by 21 px) median filter. Figure 6 shows the SEM images after the median filter was applied. The details of the images in Figures 6a and 6b correspond to the degree of noise reduction. There was less image noise removed for a median filter size of 0.1 µm by 0.1 µm as shown by the details retained in Figure 6a compared to a 0.6 µm by 0.6 µm filter in Figure 6b. The noise particles in the image appeared as bright as the eutectic phase so subsequent steps to the noise reduction step counted the retained noise as part of the eutectic network. For a smaller filter size (0.1 µm by 0.1 µm), excessive noise in the image resulted in the edges of these unwanted features to be detected as shown in Figure 7a. For a larger window size (0.6µm by 0.6µm) in Figure 7b, there was less noise particles that were included in the eutectic measurement; however, some real details such as the edges of fine primary α-Al that is about 2 µm in diameter were unintentionally removed and were not counted as primary α-Al phase. The resulting output images for both median filter sizes are shown in Figure 8.

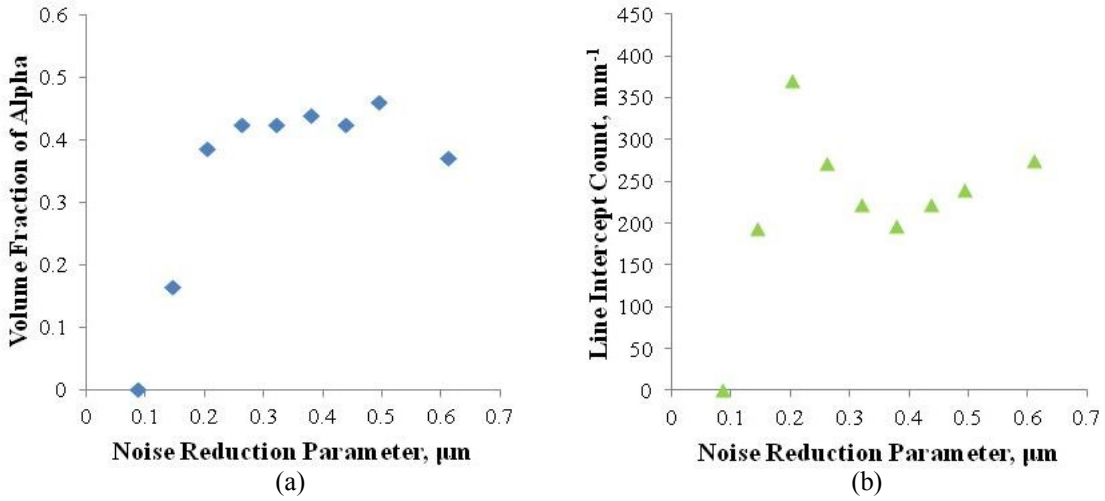

Figure 5. (a) Volume fraction of primary α-Al and (b) line intercept count as functions of the noise reduction parameter value. Range filter size was 0.1 µm by 0.1 µm (5 px by 5 px), dilation/erosion disk size was 0.3 µm (10 px), and hole close was 120 µm^2 (4096 px^2).

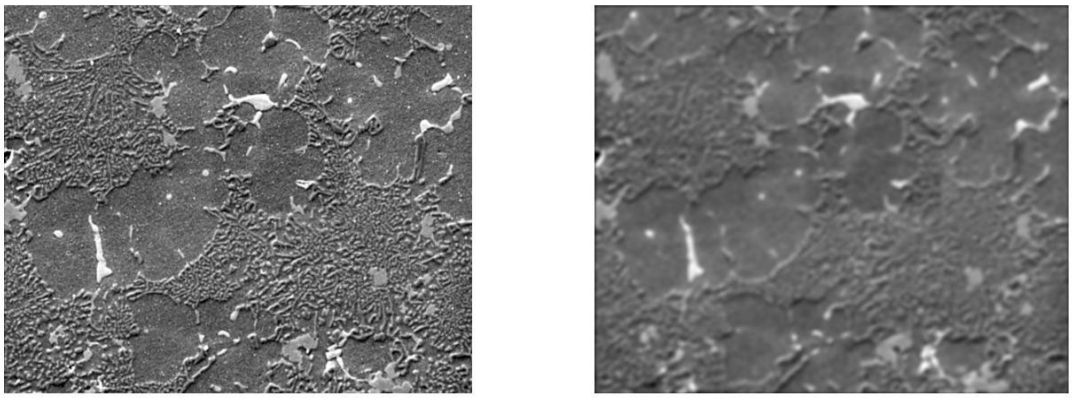

(a) (b)

Figure 6. Secondary SEM image with a resolution of 17 px/µm after the image noise reduction step for (a) a median filter size of 0.1 µm by 0.1 µm and (b) 0.6 µm by 0.6µm.

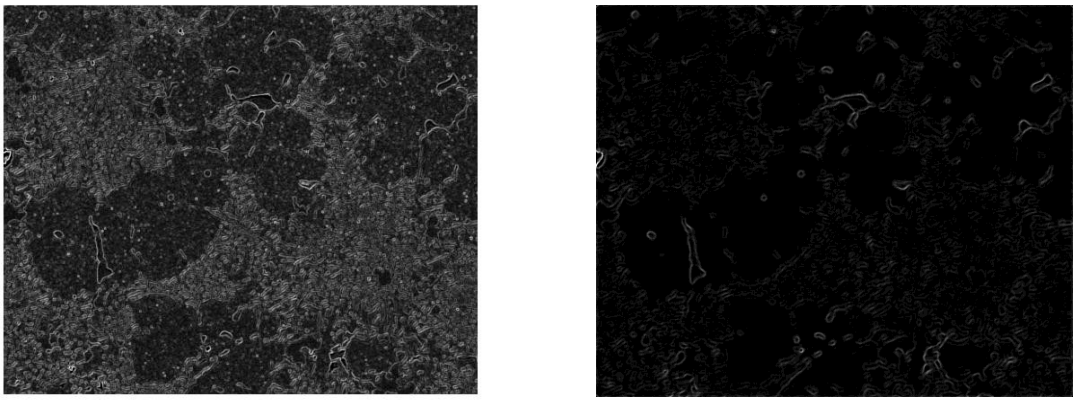

(a) (b)

Figure 7. Secondary SEM image with a resolution of 17 px/µm after the median and range filters were applied for (a) a median filter size of 0.1 µm by 0.1 µm and (b) 0.6 µm by 0.6µm. Range filter size was 0.1 µm by 0.1 µm (5 px by 5 px).

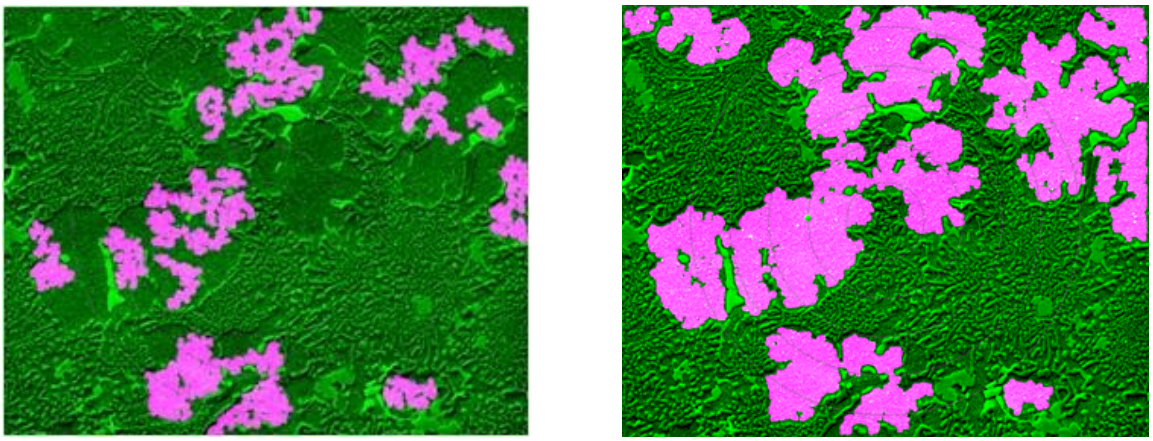

(a) (b)

Figure 8. Output image for image resolution of 17 px/µm for (a) a median filter size of 0.1 µm by 0.1 µm and (b) 0.6 µm by 0.6µm. Range filter size was 0.1 µm by 0.1 µm (5 px by 5 px), dilation/erosion disk size was 0.3 µm (10 px), and hole close was 120 µm^2 (4096 px^2) .The measured α-Al is highlighted in pink.

As seen in Figure 5a, the volume fraction curve started to plateau at about 0.2 to 0.5 µm (7 to 17 px). This plateau seems to correlate with the range of noise reduction values at which output results will not vary significantly. It must be noted, however, that this behavior was not observed in the line intercept count as shown in Figure 5b. This seems to be due to the rough edges of the α-Al cells which might have been affected by the dilation/erosion disk structuring element.

3.1.2. Edge Detection

Table 4 shows the values used for this study.

Table 4. Values Used for Parameter Study with Edge Detection as Variable

Noise Reduction		Edge Detection		Dilation/Erosion		Hole Close	
µm	px	µm	px	µm	px	μm^2	px^2
0.3	11	0.1 – 3	3 – 101	0.3	10	120	4096

Compared to the effect of the noise reduction parameter, the volume fraction and the line intercept count are less sensitive to the value of the edge detection parameter as shown in Figures 9a and 9b.

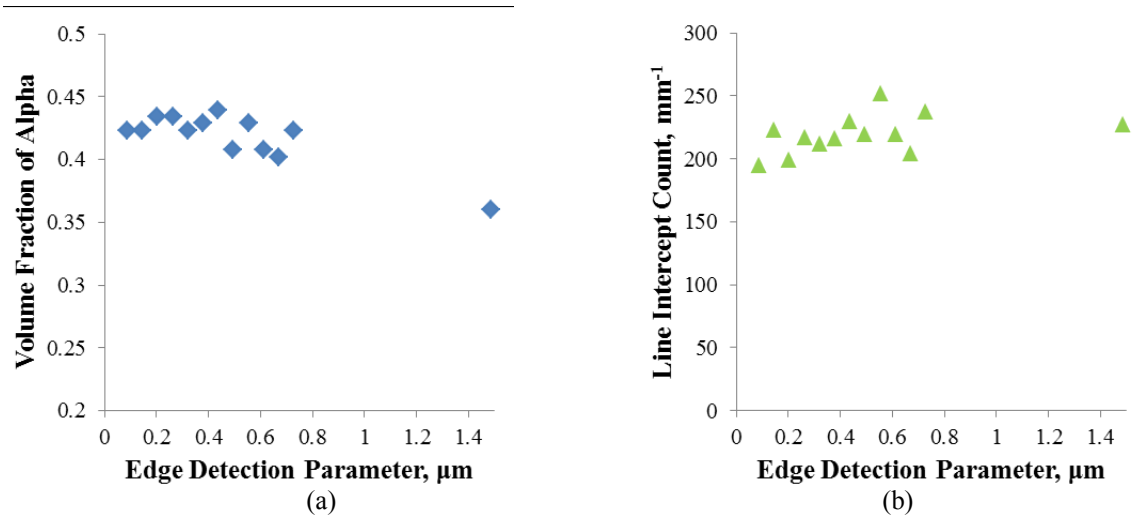

Figure 9. (a) Volume Fraction of primary α-Al and (b) line intercept count as a function of edge detection parameter value. Median filter size was 0.3 µm by 0.3 µm (11 px by 11 px), dilation/erosion disk size was 0.3 µm (10 px), and hole close was 120 μm^2 (4096 px^2).

As shown in Figure 10, the primary α-Al phase being counted was slightly smaller for a range filter of 0.7µm by 0.7µm (25px by 25px) compared to the smaller filter size (0.08 µm by 0.08 µm or 3 px by 3 px). This was due to the boundaries of the eutectic network that expanded into the primary α-Al regions which was more evident

after the the image was thresholded in Figure 11. Figures 12a and 12b show the output for range filter size of 0.08 µm by 0.08 µm (3 px by 3px) and 0.7 µm by 0.7 µm (25 px by 25 px), respectively.

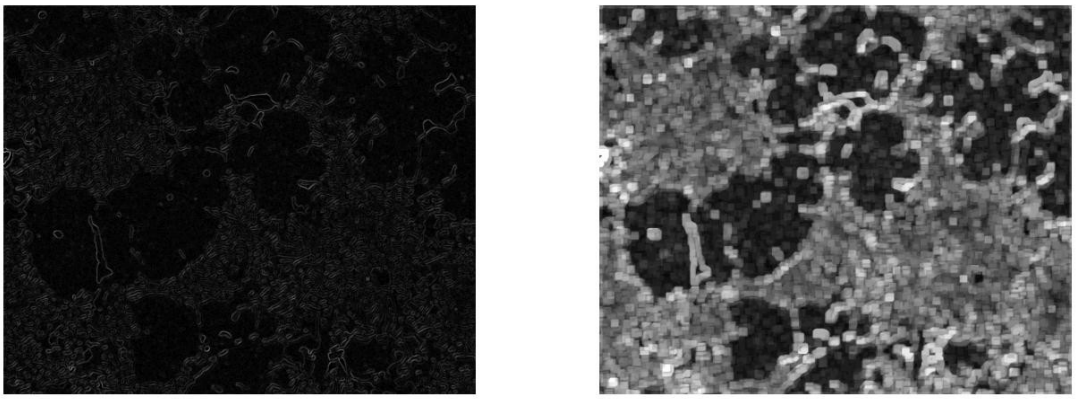

(a) (b)

Figure 10. Secondary SEM image with a resolution of 17 px/µm after the median and range filters were applied for (a) a range filter size of 0.08 µm by 0.08 µm and (b) 0.7 µm by 0.7 µm. Median filter size was 0.3 µm by 0.3 µm (11 px by 11 px).

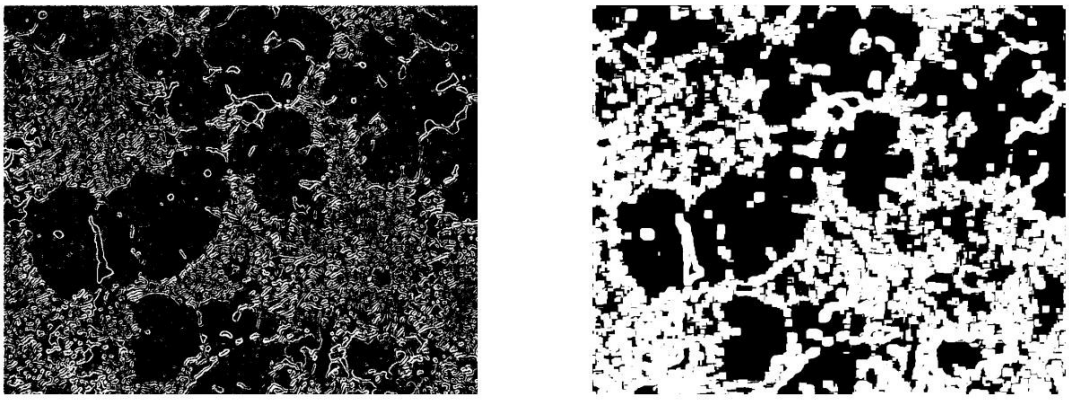

(a) (b)

Figure 11. Thresholded image for SEM image with a resolution of 17 px/µm after the median and range filters were applied for (a) a range filter size of 0.08 µm by 0.08 µm and (b) 0.7 µm by 0.7 µm. Median filter size was 0.3 µm by 0.3 µm (11 px by 11 px).

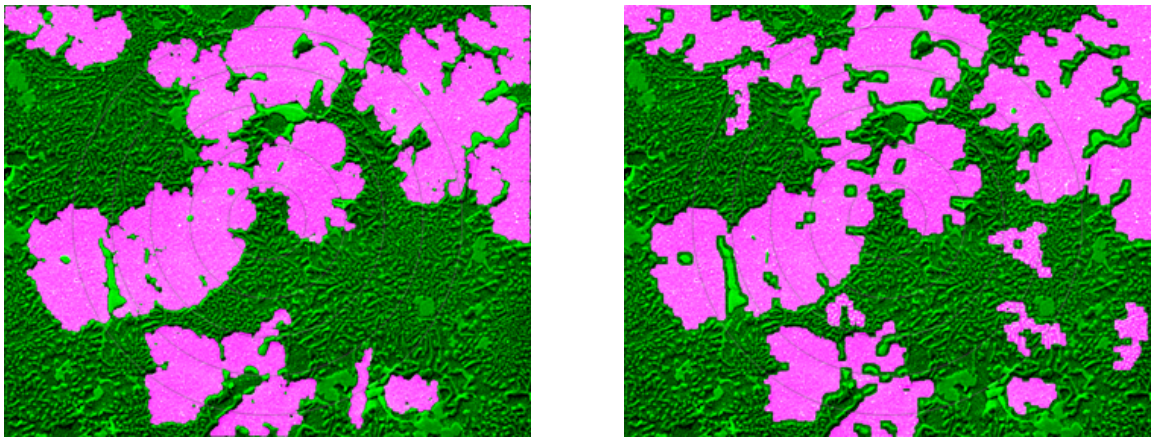

(a) (b)

Figure 12. Output image for image resolution for 17 px/µm with range filter size of (a) 0.08µm and (b) 0.7 µm. Median filter size was 0.3 µm by 0.3 µm (11 px by 11 px), dilation/erosion disk size was 0.3 µm (10 px), and hole close was 120 µm^2 (4096 px^2). The measured α-Al is highlighted in pink.

This overcounting of the eutectic phase can be explained by looking at the example pixel values presented in Table 5. It must be noted that these values do not correspond to the actual values of the SEM image being discussed in this section. These random values are examples of gray level values of an image. They typically range from 0 to 255 with 0 as a dark phase and 255 as a bright phase. The boundary between a primary α-Al cell and an eutectic network can be visualized by this set of pixel values where the α-Al corresponding to low gray level values. After applying the range filter, if the filter size was 3 px by 3 px, some dark regions were still retained as seen in Table 6. In Table 7 where the range filter size was 7 px by 7 px, the low valued pixels were transformed to a higher value (i.e., edges of eutectic network expanded to the primary α-Al regions).

Table 5. Example of a Set of Gray Level Pixel Values for an SEM Image

1	11	14	3	201	211	178
5	13	11	150	190	199	21
200	20	3	221	179	230	15
179	3	22	200	200	197	11
10	1	21	170	213	222	25
5	15	7	219	245	250	6
21	11	15	240	22	213	180

Table 6. Modified Gray Level Pixel Values for an SEM Image after Application of Range Filter with a Size of 3 by 3 pixels

13	14	150	201	211	211	211
200	199	218	218	227	215	230
200	197	218	218	80	219	230
200	199	220	218	60	219	230
179	178	218	238	80	244	250
21	20	239	238	228	244	250
21	21	240	245	250	250	250

Table 7. Modified Gray Level Pixel Values for an SEM Image after Application of Range Filter with a Size of 7 by 7 pixels

221	221	230	230	230	230	230
221	221	230	230	230	230	230
221	245	250	250	250	250	250
240	245	250	249	250	250	250
240	245	250	250	250	250	250
240	245	250	250	250	250	250
240	245	250	250	250	250	250

3.1.3. Dilation and Erosion

Table 8 summarizes the set of values used in this parameter study.

Table 8. Values Used for Parameter Study with Dilation/Erosion as Variable

Noise Reduction		**Edge Detection**		**Dilation/Erosion**		**Hole Close**	
μm	px	μm	px	μm	px	μm^2	px^2
0.3	11	0.1	5	0.6 – 6	2 – 200	120	4096

As shown in Figures 13a and 13b, at values below 0.2μm, higher volume fractions of primary α-Al were being counted. Between about 0.2 and 0.4 μm, the volume fraction and line intercept count started to plateau. At larger disk size, the algorithm started to over-count the eutectic phase. The dilation process is more critical than the erosion since the former ensures the eutectic layers will be connected and counted as a single phase.

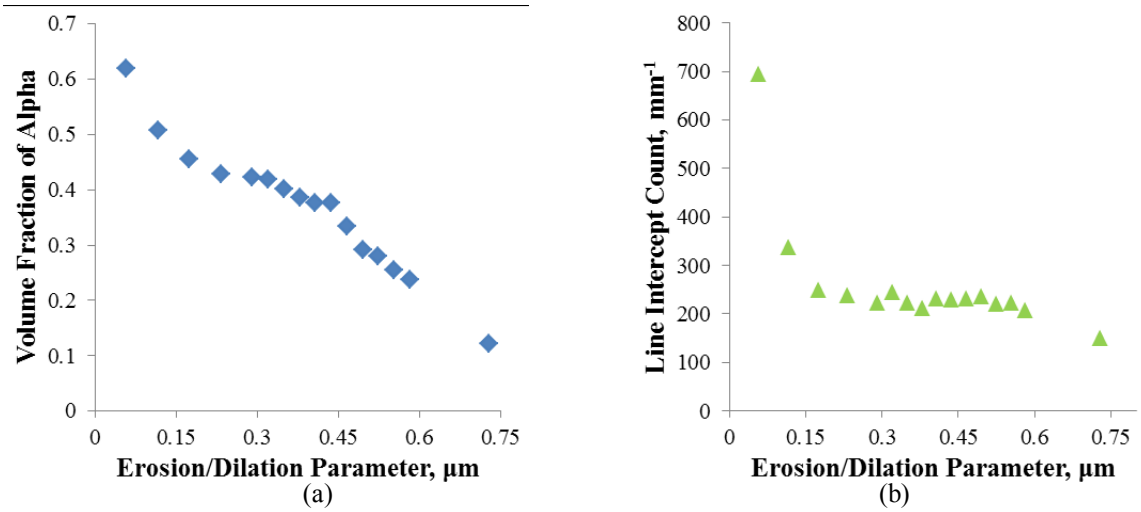

Figure 13. (a) Volume fraction of primary α-Al and (b) line intercept count as a function of dilation and erosion disk size. Median filter size was 0.3 µm by 0.3 µm (11 px by 11 px), range filter size was 0.1 µm by 0.1 µm (5 px by 5 px), and hole close was 120 µm^2 (4096 px^2).

The effect of increasing size of the dilation/erosion disk on the output image is shown in Figures 14 to 16 by comparing a disk structuring element size of 0.1 µm (4 px) and 0.6 µm (20 px). Figure 14 shows the thresholded image after the median and range filters were applied. For a disk size of 0.1 µm (4 px) in Figure 15a, there were some eutectic regions that were counted as α-Al. The dilation process was not enough to fill in the gaps in between some eutectic lamella due to the smaller structuring element. At 0.6 µm (20 px) disk size in Figure 15b, the dilation resulted in some fine α-Al being closed off and counted as eutectic. Figure 16 shows the final output image for both cases.

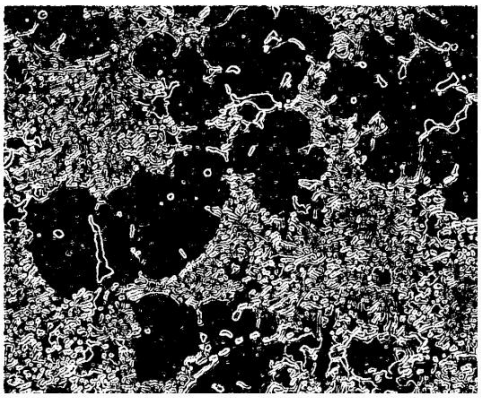

Figure 14. Thresholded image for SEM image with a resolution of 17 px/µm after the median and range filters were applied. Median filter size was 0.3 µm by 0.3 µm (11 px by 11 px) and range filter size was 0.1 µm by 0.1 µm (5 px by 5 px).

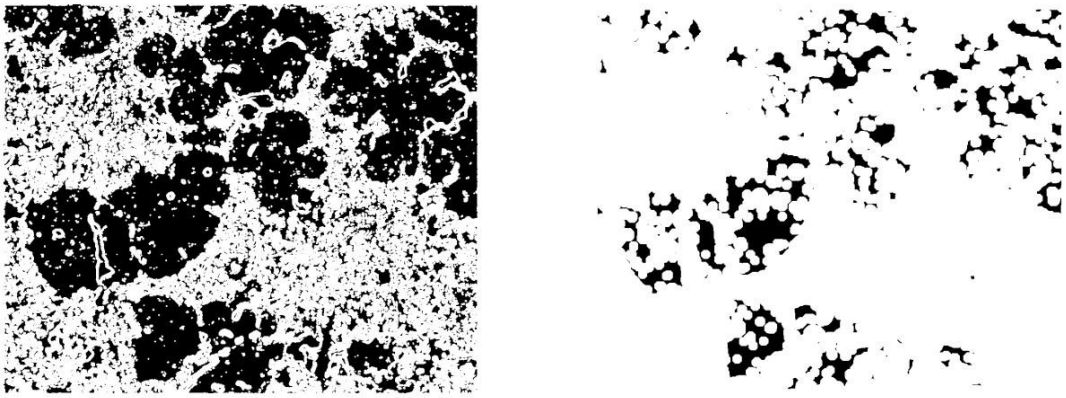

(a) (b)

Figure 15. Dilated image for a disk structuring element size of (a) 0.1 µm and (b) 0.6 µm. Median filter size was 0.3 µm by 0.3 µm (11 px by 11 px) and range filter size was 0.1 µm by 0.1 µm (5 px by 5 px).

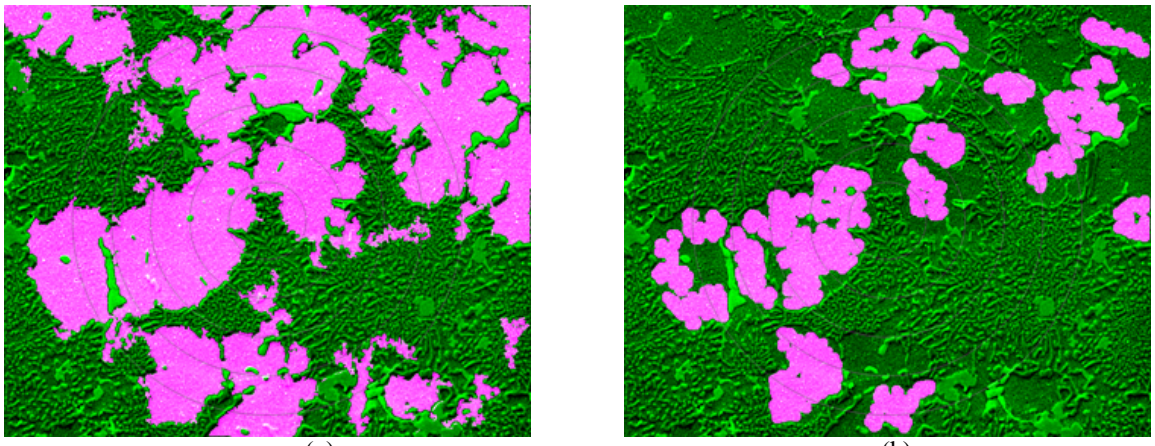

(a) (b)

Figure 16. Output image for image resolution of 17 px/µm with dilation/erosion disk size of (a) 0.1µm and (b) 0.6 µm. Median filter size was 0.3 µm by 0.3 µm (11 px by 11 px), range filter size was 0.1 µm by 0.1 µm (5 px by 5 px), and hole close was 120 µm^2 (4096 px^2). The measured α-Al is highlighted in pink.

3.1.4. Hole Close

The range of values used in this study is summarized in Table 9.

Table 9. Values Used in Parameter Study with Hole Close as Variable

Noise Reduction		**Edge Detection**		**Dilation/Erosion**		**Hole Close**	
µm	px	µm	px	µm	px	µm^2	px^2
0.3	11	0.1	5	0.3	10	30 - 6000	1000 – 2×10^5

Similar to the edge detection parameter, the plateaus observed in the volume fraction and line intercept count curves have a wider range as seen in Figures 17a and 17b. Two data points on these curves were compared in Figures 18 to 20. The dilated image is presented in Figure 18. For a hole cut off area of 3 μm^2, some eutectic lamella gaps were not closed as shown in Figure 19a. As evident in Figure 19b, for hole close area of 1500 μm^2, most α-Al cells were still being counted; however, fine α-Al cells were not. Since the cutoff area of holes to close was too high, these small α-Al particles were closed and counted as eutectic. The output images are shown in Figure 20.

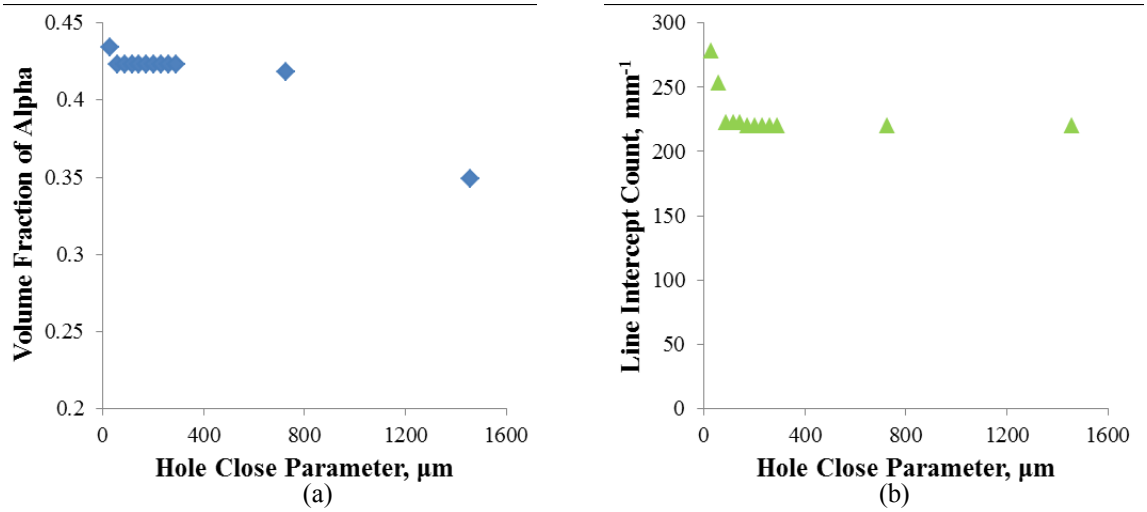

Figure 17. (a) Volume fraction of primary α-Al and (b) line intercept count as a function of hole close parameter. Median filter size was 0.3 µm by 0.3 µm (11 px by 11 px), range filter size was 0.1 µm by 0.1 µm (5 px by 5 px), and dilation/erosion disk size was 0.3 µm (10 px).

Figure 18. Image after the dilation step. Median filter size was 0.3 µm by 0.3 µm (11 px by 11 px), range filter size was 0.1 µm by 0.1 µm (5 px by 5 px), and dilation/erosion disk size was 0.3 µm (10 px).

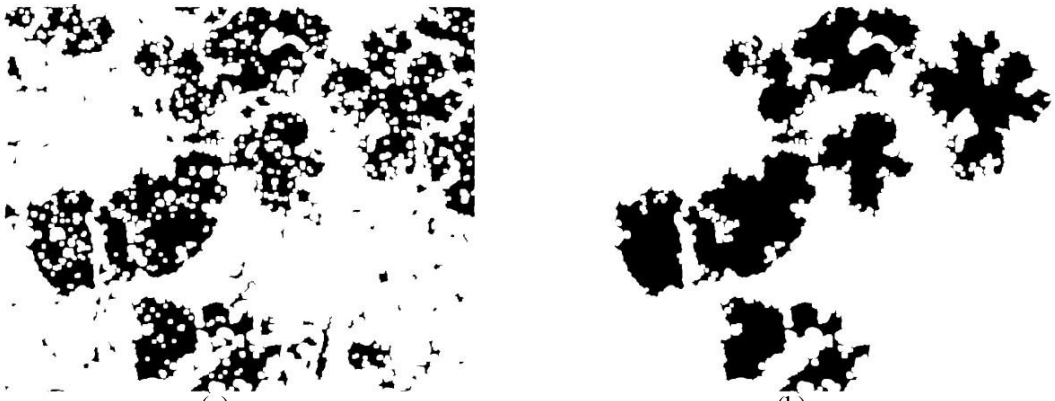

(a) (b)

Figure 19. Image after small holes/gaps within phases in the dilated image were closed for hole close area of (a) 3 µm^2 and (b) 1500 µm^2. Median filter size was 0.3 µm by 0.3 µm (11 px by 11 px), range filter size was 0.1 µm by 0.1 µm (5 px by 5 px), and dilation/erosion disk size was 0.3 µm (10 px).

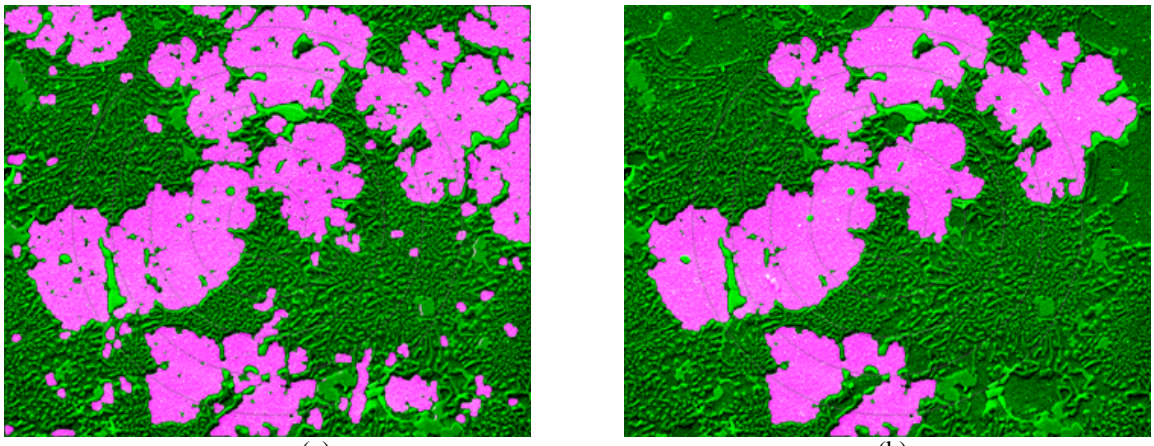

(a) (b)

Figure 20. Output image for image resolution of 17 px/µm for hole close area of (a) 3µm^2 and (b) 800 µm^2. Median filter size was 0.3 µm by 0.3 µm (11 px by 11 px), range filter size was 0.1 µm by 0.1 µm (5 px by 5 px), and dilation/erosion disk size was 0.3 µm (10 px). The measured α-Al is highlighted in pink.

It must be noted that the hole close parameter value chosen must depend on the dilation disk size. If the dilation size is large enough to minimize the gaps in between eutectic lamella, then the cutoff area can be as small as a eutectic lamella. This way, fine α-Al cells will not be distinguished as part of the eutectic regions.

3.1.5. Input Parameter Values

From the studies discussed in the previous sections, the range of acceptable values for each parameter is summarized in Table 10.

Table 10. Range of Values for Each Parameter Determined from Preliminary Parameter Studies

Parameter	Range of Values	Unit
Noise Reduction	0.2 – 0.5	µm
Edge Detection	0.1 – 0.4	µm
Dilation/Erosion	0.2 – 0.4	µm
Hole Close	60 – 1000	µm^2

As previously mentioned, the value of the noise reduction must be small enough to prevent elimination of fine intermetallics. The smallest Fe-rich phase in this alloy was about 0.7 μm; the range of the filter window size would work in reducing the noise without removing necessary features. The edge detection parameter must be relatively smaller than the fine α-Al cells; the values specified in Table 10 would be able to detect eutectic lamella and fine α-Al. The dilation disk should be small enough to avoid closing small α-Al cells, the finest of which has a radius of about 1.7 μm. The hole close area cutoff must depend on the dilation value to avoid closing of some α-Al cells.

3.2. Measurement Results as a Function of Resolution and Magnification

While the actual size of any microstructural feature is independent of the magnification or the resolution of the image, the size of a feature measured at different resolutions, whether the measurement is done manually or is computer-aided, may not be the same. At lower resolutions and magnifications, some fine features may be missed and undercounted. On the other hand, at higher resolutions and magnifications, the measurement might not be an accurate representative of the area of interest since the field of view might be too narrow to see enough features.

The appropriate resolution at which analysis must be done depends on the size of the feature of interest. However, there should be a range of resolution where microstructural measurements become statistically similar. Figure 21 shows the volume fraction of α-Al at different resolutions or length scales for optical and SEM images. At SEM resolution of about 3 px/μm, the amount of α-Al was significantly higher than measurements done on higher resolutions. The curve started to plateau at about 6 px/μm.

It must be noted, however, than the deviation of each data set increased at higher resolution which was due to the limitation in image area.

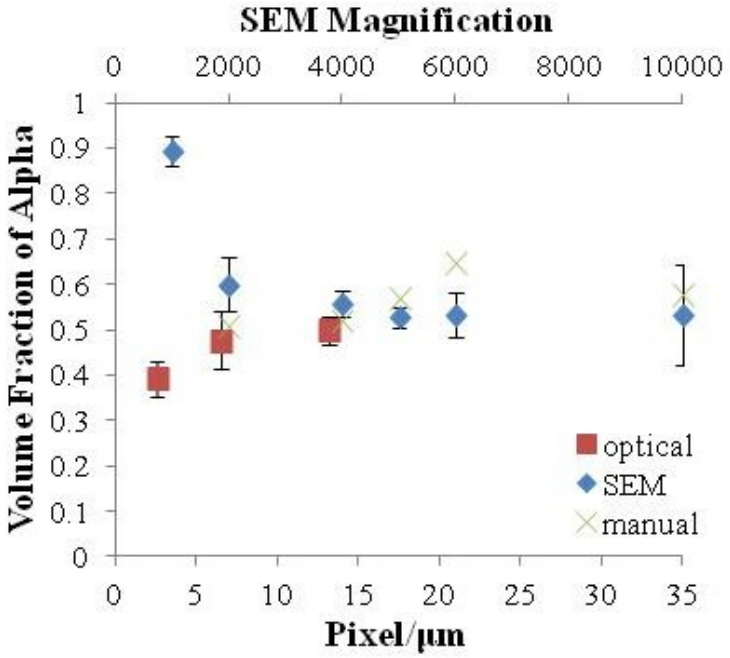

Figure 21. Volume fraction of primary α-Al as function of image resolution or length scale. Median filter size was 0.3 µm by 0.3 µm, range filter size was 0.3 µm by 0.3 µm, dilation/erosion disk size was 0.3 µm, and hole close was 120 µm^2.

Based on Figure 21, the volume fraction curve started to plateau at about 6 px/µm. Looking at pixel resolution of 3 px/µm, the primary α-Al was overcounted. An alternative technique was considered in order to analyze this data point. The Canny edge detection method was used and compared to the range filter edge detection technique used in this study. In the former technique, the value of the central pixel was replaced by the weighted average of its neighborhood, the size of which depends on the input σ. It was found out that even with the Canny method, the amount of the primary α-Al was still inaccurate. The α-Al cells were undercounted as seen in the curve in Figure 22. Figure 23a and 23b show the output images for the range filter edge detection method and

Canny edge technique, respectively. Regardless of the edge detection technique, at 3 px/µm, there is not enough contrast for the algorithm to distinguish the features from each other.

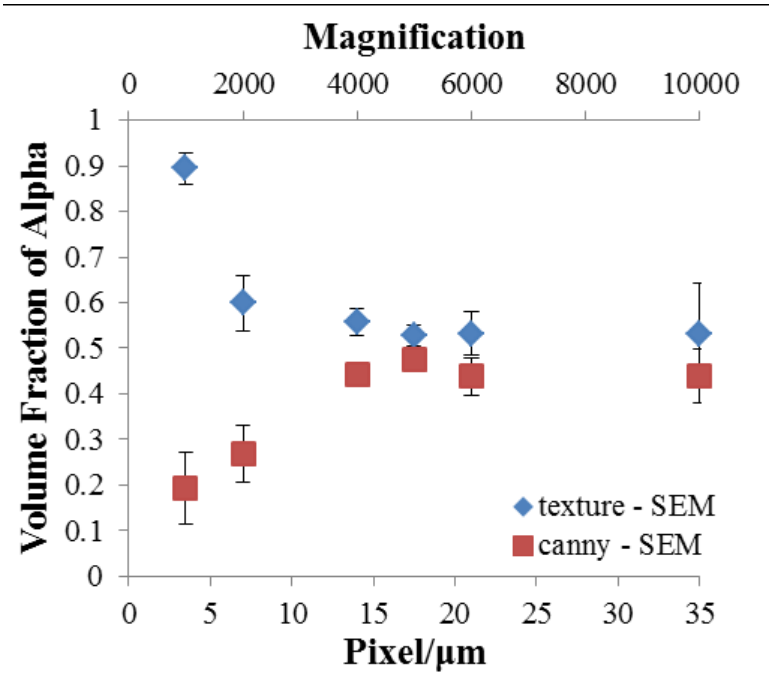

Figure 22. Volume fraction of primary α-Al as function of pixel resolution or length scale for different edge detection technique (texture analysis vs Canny edge detection method). Median filter size was 0.3 µm by 0.3 µm, range filter size was 0.3 µm by 0.3 µm, dilation/erosion disk size was 0.3 µm, and hole close was 120 µm^2. The Canny sigma value was 0.3 µm.

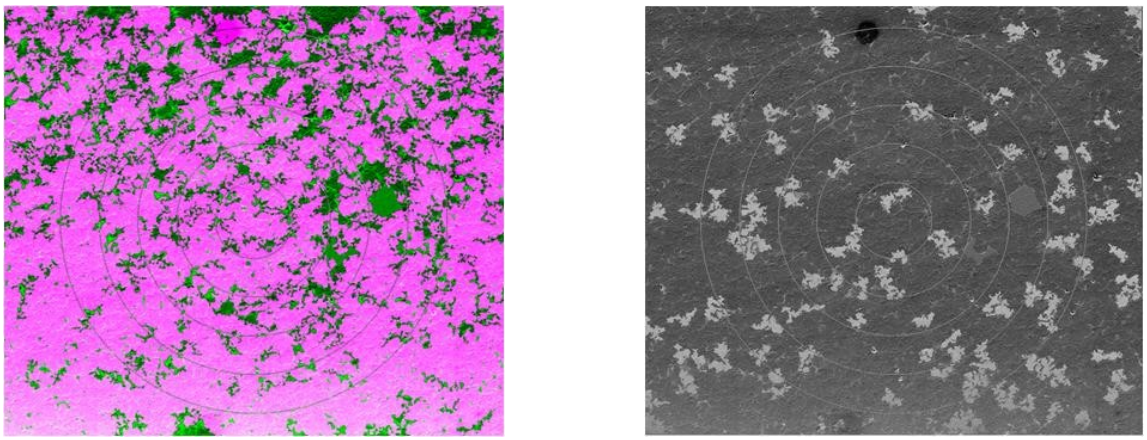

(a) (b)

Figure 23. Output images for SEM image with a pixel resolution of 3 px/µm for analyses that used (a) range filter and (b) Canny edge as the edge detection technique. Median filter size was 0.3 µm by 0.3 µm, range filter size was 0.3 µm by 0.3 µm, dilation/erosion disk size was 0.3 µm, and hole close was 120 µm^2. The Canny sigma value was 0.3 µm.

Going back to the volume fraction curve in Figure 21, it was observed that the curves for the SEM images and optical micrographs exhibited opposing behavior. At SEM lower resolutions, the primary α-Al was overcounted while for optical lower resolutions, there was less primary α-Al measured. Figure 24a and 24b shows the output images for these two cases. The primary α-Al appears darker in SEM images while it is brighter than the eutectic phase in optical micrographs.

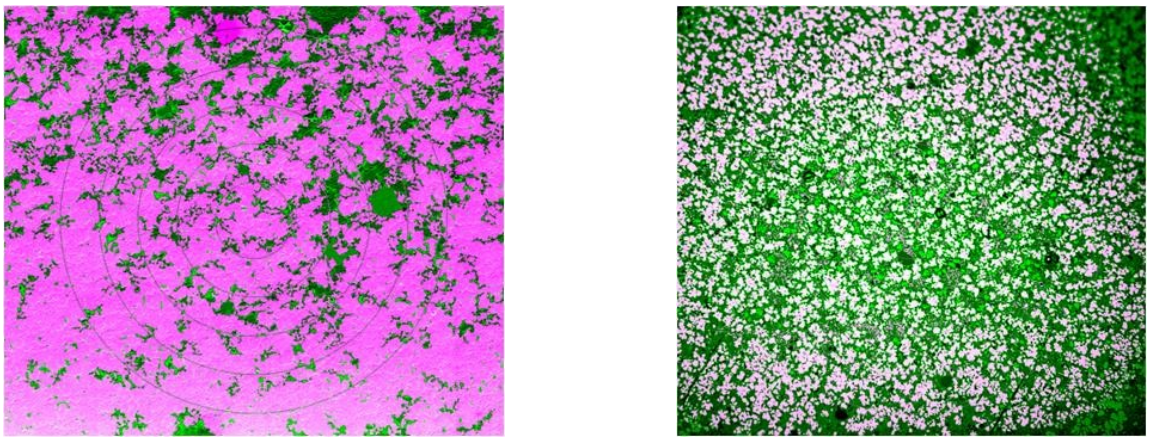

(a) (b)

Figure 24. Output image of (a) SEM image with pixel resolution of 3 px/µm and (b) optical microscope image with pixel resolution of 3 px/µm. Median filter size was 0.3 µm by 0.3 µm, range filter size was 0.3 µm by 0.3 µm, dilation/erosion disk size was 0.3 µm, and hole close was 120 µm^2.

The curve plateau observed at image resolutions of 6 to 35 px/µm in Figure 21 was also exhibited in Figure 25 although not as noticeable. The volume fraction measured by the algorithm had a good correlation with the representative manual measurements. The line intercept count, however, had a relatively higher deviation from the manual values. This was due to the rough edges of the α-Al cells. Figure 26a shows a higher magnification image of a location in the sample. As seen in Figure 26b, the edges of the α-Al cells were much less smooth.

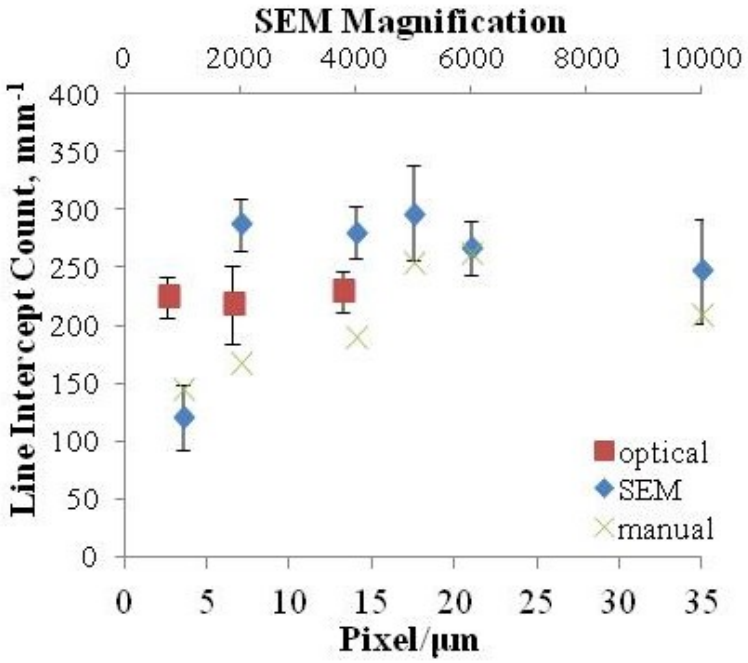

Figure 25. Line intercept count as function of image resolution or length scale. Median filter size was 0.3 µm by 0.3 µm, range filter size was 0.3 µm by 0.3 µm, dilation/erosion disk size was 0.3 µm, and hole close was 120 µm^2. The Canny sigma value was 0.3 µm.

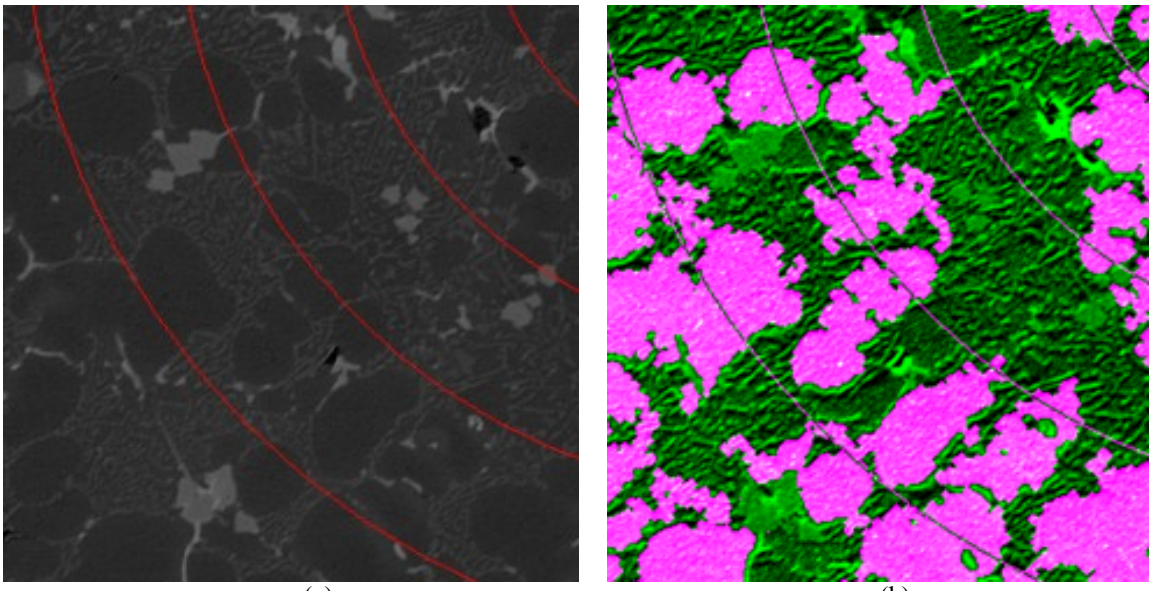

(a) (b)

Figure 26. (a) Backscatter electron SEM image with pixel resolution of 6 pixel/µm of the same location in (b) the output image measured by the algorithm. Median filter size was 0.3 µm by 0.3 µm, range filter size was 0.3 µm by 0.3 µm, dilation/erosion disk size was 0.3 µm, and hole close was 120 µm^2. The Canny sigma value was 0.3 µm.

4. FUTURE WORK

4.1. Image Analysis

The analysis presented in the previous sections was done on one sample with an approximated secondary dendrite arm spacing of about 5μm. The goal of this research is for the proposed microstructural characterization method to be applicable to other aluminum HPDC alloys as well as other metal castings. The plateau observed in the volume fraction curve is expected to change with the feature size of a particular casting. For a coarser microstructure such as a sand casting, the acceptable image resolution is most likely lower than the one presented here. For a much finer microstructure, the minimum resolution will shift to a higher value.

The next step in the improvement of the algorithm is to be able to guide the user on where his analysis is relative to the acceptable range. It can be done by downscaling an input image and giving out output measurements for the original image resolution and for a coarser resolution. For example, if the image is at 10 px/μm, the algorithm will do the analysis at this resolution, at 5 px/μm, and at 2.5 px/μm. If the volume fraction and line intercept count values are statistically the same, then the resolution initially chosen by the user lies on the corresponding curve plateau previously discussed.

Smoothing of the edges of the primary α-Al must also be done to decrease the intercepts being counted by the algorithm. That way, the deviation between the output values and the manual measurements will be minimized. Performing multiple dilation and erosion using a smaller disk size may help with improving these edges. Removal of the hole-closing step so the dilation and erosion will be done one after another might improve the output results.

It will also be beneficial if the range of parameter values obtained from the studies will be statistically analyzed to determine whether parameters are dependent on each other or not and to find if there is an optimum set of value for each.

Testing of the accuracy of this automated approach must also be done by using the algorithm on other set of images of castings with a coarser microstructure and known volume fraction and dendrite cell size or arm spacing.

4.2. Microstructural Analysis

To improve image quality, samples may be remounted using a material with better edge retention. This will allow for well-focused micrographs along the cast surface. It must be noted that proper polishing of the samples is extremely important since the algorithm is still sensitive to unwanted coarse features.

Conducting measurements on other areas of the casting must also be done to determine the effect of distance from cast surface and distance from the gate on the resulting microstructure. This will serve the ultimate goal of contributing quantitative data on aluminum castings, although specifically on aluminum 380 in this case, which will be beneficial in the development of aluminum high pressure die castings in general.

5. CONCLUSIONS

Automating the microstructural analysis of aluminum high pressure die castings is relatively more efficient than the traditional manual stereology technique. In this research, the algorithm functions used were presented and analyzed. Acceptable range of values for each parameter was proposed.

The resolution at which image analysis must be done depends on the size of the features of interest. For the aluminum die casting sample examined in this study, pixel resolutions below 6 px/μm were too low for the algorithm to distinguish the phases from each other. At resolutions higher than 6 px/μm, the volume fraction of primary α-Al and the line intercept count curves plateau. Within this range, analysis can be done and comparable results will be obtained. However, at higher resolutions, the deviation and the required number of images necessary to reach a 5% coefficient of variation are significantly higher than resolutions at the onset of the curve plateau.

6. GENERAL REFERENCES

1. E.J. Vinarcik, "High Integrity Die Casting Processes," John Wiley & Sons, New York, pp 5-8, 2003.

2. C.M Gourlay, H.I. Laukli, A.K. Dahle, "Defect Band Characteristics in Mg-Al and Al-Si High-Pressure Die Castings," Metallurgical and Materials Transactions A, vol. 38A, pp 1833-1844, 2007.

3. N. Tsumagari, J.R. Brevick, C.E. Mobley, "Control of Microstructures in Aluminum Alloy Diecastings," AFS Transactions, vol. 106, pp 15-20, 1998.

4. S. Sannes, H. Gjestland, H. Westengen, H.I. Laukli, O. Lohne, "Magnesium Die Casting for High Performance," 6th International Conference on Magnesium Alloys and Their Applications, K.U. Kainer, ed., Werkstoff-Informationgesellschaft, Frankfurt, Germany, pp 725-731, 2003 Cited in C.M Gourlay, H.I. Laukli, and A.K. Dahle, "Defect Band Characteristics in Mg-Al and Al-Si High-Pressure Die Castings," Metallurgical and Materials Transactions A, vol. 38A, pp 1833-1844, 2007.

5. S. Otarawanna, C.M. Gourlay, H.I. Laukli, A.K. Dahle, "Microstructure Formation in AlSi4MgMn and AlMg5Si2Mn High-Pressure Die Castings," Metallurgical and Materials Transactions A, vol. 40A, pp 1645-1659, 2009.

6. Z.W. Chen, "Skin Solidification During High Pressure Die Casting of Al-11Si-2Cu-1Fe Alloy," Materials Science and Engineering A, vol. 348, pp 145-153, 2003.

7. C. Pitsaris, T. Abbott, C.J. Davidson, "The Formation of Defect Bands in Magnesium Die Castings," First International Light Metals Technology Conference, A.K. Dahle, ed., CAST CRC, Brisbane, Austalia, pp 223-226, 2003, cited in C.M Gourlay, H.I. Laukli, and A.K. Dahle, "Defect Band Characteristics in Mg-Al and Al-Si High-Pressure Die Castings," Metallurgical and Materials Transactions A, vol. 38A, pp 1833-1844, 2007.

8. P.D.D. Rodrigo, V. Ahuja, "Effect of Casting Parameters on the Formation of 'Pore/Segregation Bands' in Magnesium Die Castings," Proceedings of the Second Israeli Conference on Magnesium Science and Technology, Dead Sea, Magnesium Research Institute, Beer-Sheva, Israel, 2000, E. Aghion and D. Eliezer, eds., pp 97-104, 2000, cited in C.M Gourlay, H.I. Laukli, and A.K. Dahle, "Defect Band

Characteristics in Mg-Al and Al-Si High-Pressure Die Castings," Metallurgical and Materials Transactions A, vol. 38A, pp 1833-1844, 2007.

9. H.I. Laukli, C.M. Gourlay, A.K. Dahle, "Migration of Crystals During the Filling of Semi-Solid Castings," Metallurgical and Materials Transactions A, vol. 36A, no. 3A pp 805-818, 2005.

10. C.M. Gourlay, A.K. Dahle, "Dilatant Shear Bands in Solidifying Metals," Nature, vol. 445, pp 70-73, 2007.

11. T. Sumitomo, D.H. St. John, T. Steinberg, "The Shear Behaviour of Partially Solidified Al-Si-Cu Alloys," Materials Science and Engineering A, vol. 289, pp 18-29, 2000.

12. C.M. Gourlay, H.I. Loukli, A.K. Dahle, "Segregation Band Formation in Al-Si Die Castings," Metallurgical and Materials Transactions A, vol. 35A, no. 91, pp 2881-2891, 2004.

13. H.I. Laukli, C.M. Gourlay, A.K. Dahle, O. Lohne, "Effects of Si Content on Defect Band Formation in Hypoeutectic Al-Si Die Castings," Materials Science and Engineering A, vol. 413-414, pp 92-97, 2005.

14. B.P. Bardes, M.C. Flemings, "Dendrite Arm Spacing and Solidification Time in a Cast Aluminum-Copper Alloy," AFS Transactions, vol. 74, pp 406-412, 1966.

15. R.E. Spear, G.R. Gardner, "Dendrite Cell Size," AFS Transactions, vol. 71, pp 209-215, 1963.

16. M.C. Flemings, "Solidification Processing," McGraw-Hill, New York, NY, pp 246-248, 1974.

17. J.I. Cho and C. W. Kim, "The Relationship Between Dendrite Arm Spacing and Cooling Rate of Al-Si Casting in High Pressure Die Casting," International Journal of Metalcasting, vol. 8, Issue 1, pp 49-55 2014.

18. A. Bowles, K. Nogita, M. Dargusch, C. Davidson, J. Griffiths, "Grain Size Measurements in Mg-Al High Pressure Die Castings Using Electron Back-Scattered Difraction (EBSD)," Materials Transactions, vol. 45, no. 11, pp 3114-3119, 2004.

19. J.P. Weiler, J.T. Wood, R.J. Klassen, R. Berkmortel, G. Wang, "Variability of Skin Thickness in an AM60B Magnesium Alloy Die-Casting," Materials Science and Engineering A, vol. 419, pp 297-305, 2006.

20. C.H. Caceres, J.R. Griffiths, A.R. Pakdel, C.J. Davidson, "Microhardness Mapping and the Hardness-Yield Strength Relationship in High-Pressure Diecast Magnesium Alloy AZ91," Materials Science and Engineering A, vol. 402, pp 258-268, 2005.

21. A.I. Bowles, J.R. Griffiths, C.J. Davidson, TMS Magnesium Technology, Warrendale, PA, pp 161-168, 2001, cited in J.P. Weiler, J.T. Wood, R.J. Klassen, R. Berkmortel, G. Wang, "Variability of Skin Thickness in an AM60B Magnesium Alloy Die-Casting," Materials Science and Engineering A, vol. 419, pp 297-305, 2006.

22. MATLAB 6.1, The MathWorks, Inc., Natick, MA, 2000.

23. D. Zeng, "Advances in Information Technology and Industry Applications," Springer Science & Business Media, p 240, 2012.